Numerical Investigation of Sphere Cavitation Dynamics and Pressure-Wave Propagation for Underwater Noise Prediction using OpenFOAM

Downloaded from: https://research.chalmers.se, 2026-11-07 10:27 UTC

Citation for the original published paper (version of record):

Ryu, S., Cianferra, M., Everyd Bensow, R. (2026). Numerical Investigation of Sphere Cavitation Dynamics and Pressure-Wave Propagation for
Underwater Noise Prediction using OpenFOAM. 36th Symposium on Naval Hydrodynamics

N.B. When citing this work, cite the original published paper.

research.chalmers.se offers the possibility of retrieving research publications produced at Chalmers University of Technology. It covers all kind of research output: articles, dissertations, conference papers, reports etc. since 2004. research.chalmers.se is administrated and maintained by Chalmers Library

(article starts on next page)

36th Symposium on Naval Hydrodynamics
Busan, Korea, 14 – 19 June, 2026

Numerical Investigation of Sphere Cavitation Dynamics and Pressure-Wave Propagation for Underwater Noise Prediction using OpenFOAM

Seo-Yoon Ryu,[1] Marta Cianferra,[2] Rickard Bensow,[1]
([1]Chalmers University of Technology, Gothenburg, Sweden,
[2]University of Trieste, Trieste, Italy)

ABSTRACT

Cloud cavitation involves highly unsteady vapor-cloud growth and collapse, generating intense pressure pulses and broadband acoustic emissions in marine and hydraulic systems. While incompressible simulations are widely used to predict cavitation dynamics, their ability to represent collapse-induced pressure-wave propagation remains limited. In this study, a comparative computational investigation of cloud cavitation around a sphere is performed using incompressible and compressible multiphase formulations, with validation against experimental benchmark data. The influence of compressibility on cavitation behavior, pressure fluctuations, and acoustic-spectrum characteristics is systematically examined. The results indicate that resolving localized collapse events is key to capturing high-frequency pressure fluctuations.

INTRODUCTION

Cloud cavitation at low cavitation numbers is characterized by highly unsteady shedding and collapse behavior. The cyclical growth, detachment, and implosion of vapor clouds generate intense pressure fluctuations that propagate through the surrounding fluid and contribute significantly to broadband underwater noise. The collapse of vapor clouds is known to produce strong pressure pulses and shock-like structures that act as primary acoustic sources. Early theoretical and numerical studies demonstrated that the collective collapse of a bubble cloud can generate inward-propagating pressure waves and significant acoustic impulses (Wang et al., 1995).

Although computational fluid dynamics (CFD) has advanced considerably, accurately predicting both cavitation dynamics and the associated pressure-wave field remains challenging. Most numerical studies have concentrated on reproducing global cavitation features, including cavity length, shedding frequency, and vapor volume distribution, which are essential for flow validation.

However, these macroscopic quantities offer limited insight into the mechanisms responsible for collapse-induced pressure pulses and acoustic emissions.

Many existing simulations rely on incompressible flow formulations, which effectively capture overall cavitation topology while maintaining computational efficiency. However, such formulations are inherently limited in representing transient pressure-wave propagation associated with rapid collapse events. Compressible multiphase approaches provide a framework for resolving both cavitation dynamics and pressure-wave transmission within a single formulation, yet systematic comparisons between incompressible and compressible predictions of collapse-driven pressure fluctuations remain limited, particularly in cloud cavitation regimes. Numerous experimental and numerical studies have investigated the dynamics of cloud cavitation and the associated pressure fluctuations. Early theoretical work by Willson et al. (Wilson et al., 2008) described the collective collapse behavior of bubble clouds, showing that collapse often occurs in a cascading manner from the outer region toward the cloud center, leading to strong localized pressure peaks. Cloud cavitation over lifting bodies has also been widely studied in relation to vortex dynamics and re-entrant jet mechanisms. Arabnejad et al. (Arabnejad et al., 2019) performed a combined experimental and numerical study of leading-edge cavitation over a hydrofoil and identified two distinct shedding mechanisms: a primary shedding associated with periodic detachment of large vapor clouds, and a secondary shedding driven by small-scale vortex structures. These interactions between the sheet cavity, cloud cavity, and re-entrant jet were shown to play an important role in the generation of transient cavitation structures and associated pressure fluctuations.

Liu et al. (Liu et al., 2023) investigated the dynamic behavior of cloud cavitation around a flexible hydrofoil and showed that structural and flow interactions significantly influence shedding characteristics and cavity evolution. More recent compressible cavitation studies have further examined pressure statistics and collapse dynamics, highlighting the presence of shock-like pressure pulses and high-frequency pressure fluctuations associated with vapor collapse (Zhao et al., 2023).

On the numerical side, several CFD investigations have focused on predicting cavitation structures and unsteady flow features around bluff bodies and spheres. Numerical studies have also examined the unsteady characteristics of cavitating flow around spheres, including shedding dynamics, re-entrant jet interactions, and Strouhal-number-based frequency behavior (Cheng et al., 2019). Large-eddy simulation (LES) studies have demonstrated the ability of multiphase models to capture cavity shedding and wake instabilities (Pendar et al., 2018), while spectral and wavelet analyses have been used to examine the frequency content of cavitation dynamics and pressure signals around spheres (Kolahan et al., 2018). In addition, recent studies have explored the role of compressibility in cavitating flows, showing that compressible formulations can better capture transient pressure pulses and re-entrant jet dynamics compared with incompressible approaches (Wang et al., 2018).

The cavitating flow around a sphere in a water tunnel provides an effective benchmark configuration for investigating these issues. Its geometric simplicity and the availability of well-documented experimental measurements enable systematic assessment of numerical models while minimizing geometric complexity. In addition, the formation of periodic cloud cavitation and associated collapse events makes this case particularly suitable for examining the relationship between cavitation dynamics and pressure pulse generation.

Despite these advances, most existing studies primarily focus on predicting cavitation topology, vortex dynamics, and shedding behavior, while collapse-induced pressure pulses are closely related to cavitation noise generation. Acoustic analogy approaches, most notably the Ffowcs Williams–Hawkings (FWH) formulation, have been widely adopted in hybrid CFD–acoustic frameworks for predicting flow-induced noise (Ffowcs-Williams et al., 1969; Farassat, et al., 1975; Brentner et al., 1998; Farassat, et al., 2007). In marine applications, hybrid approaches combining incompressible CFD with the FWH method have been widely used to estimate cavitation-induced pressure pulses and underwater radiated noise (Vikström et al. 2022; Khraisat et al. 2026). However, the theoretical foundation of the FWH formulation is primarily derived for single-phase compressible flows, and its application to cavitating multiphase flows remains not rigorously established. In addition, the definition of the permeable integration surface, including its shape, size, and spatial placement, can significantly influence the predicted acoustic response. This sensitivity remains insufficiently explored for cloud-cavitation-dominated flows.

In this study, a high-fidelity computational investigation of cloud cavitation around a sphere is conducted with emphasis on both flow validation and acoustic-spectrum characterization. Numerical predictions are first validated against experimental data using key global indicators, including cavity length, inception angle, and temporal variability. The differences between incompressible and compressible formulations are then examined to assess their impact on cavitation dynamics and pressure fluctuation characteristics. Furthermore, both near-field pressure signals and far-field acoustic spectra are analyzed to establish the connection between collapse-induced pressure sources and radiated acoustic signatures. A cross-tool comparison using OpenFOAM and STAR-CCM+ is also performed to evaluate the sensitivity of predicted cavitation behavior and pressure fluctuations to solver formulation and numerical treatment.

Experimental configuration and Computational domain

To investigate the influence of flow compressibility and numerical formulation on cavitation dynamics and pressure-wave propagation, a computational framework was established to replicate the water-tunnel experiments of cloud cavitation around a sphere (Brandner P.A. et al., 2010; De Graaf et al., 2017).

Both incompressible and compressible formulations were employed to enable a systematic comparison of cavitation behavior and pressure fluctuations. Incompressible simulations were conducted using OpenFOAM and STAR-CCM+ to establish a consistent baseline and assess solver-dependent numerical effects. In contrast, compressible simulations were performed in OpenFOAM to resolve transient pressure-wave propagation associated with vapor collapse.

The numerical setup closely follows the experimental configuration in terms of geometry, operating conditions, and flow regime. The computational domain represents the rectangular water-tunnel test section with a cross-sectional area of 0.6×0.6 m, extending 0.75 m upstream and 1.85 m downstream of the sphere center, as illustrated in Figure 1. The sphere diameter was set to $D = 0.15$ m, with a uniform inflow velocity of $U_\infty = 9$ m/s , corresponding to a Reynolds number of $Re = 1.5 \times 10^6$ .The cavitation number is controlled by adjusting the outlet static pressure according to:

$$\sigma = \frac{2(p_\infty - p_v)}{\rho U_\infty^2} \qquad (1)$$

where p_∞ is the reference pressure, p_v is the saturation vapor pressure, and ρ is the liquid density.

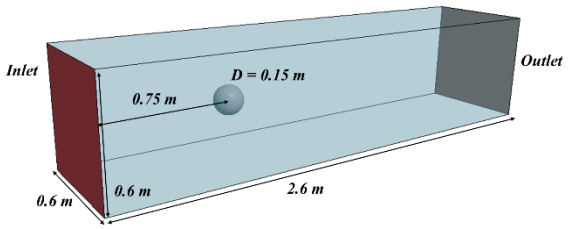

Figure 1: Configuration of the computational domain with a sphere in the water tunnel.

The cavitation number $\sigma = 0.4$ was considered to represent a developed cavitation regime. The computational grid was constructed using a trimmed/hexa-dominant topology with local refinement in the vicinity of the sphere and in the wake region, where cloud shedding and collapse are expected.

Prism layers were applied on the sphere surface to accurately resolve near-wall gradients and to support the turbulence modeling approach. The prism-layer configuration consisted of 14 layers with controlled growth rates to ensure appropriate wall-normal resolution. A grid-dependency study was performed by varying both the bulk mesh resolution and the near-wall refinement level. This enabled the sensitivity of predicted cavitation characteristics, including cavity length and inception angle, to be systematically assessed.

Accurate prediction of cloud cavitation dynamics requires sufficient spatial resolution to capture highly localized and transient collapse events. Since collapse-induced pressure pulses are strongly dependent on local flow features, it is essential to quantify the sensitivity of both cavitation behavior and the associated pressure response to spatial discretization.

In the present study, two complementary grid refinement strategies were adopted to assess resolution effects systematically: (i) global mesh refinement and (ii) near-wall resolution refinement. For the global refinement study, the bulk cell size in the refined region surrounding the sphere was varied such that the characteristic resolution satisfied D/Δx = 25, 75, and 100, while maintaining a fixed prism-layer configuration consisting of 14 layers with a target wall-normal resolution of $y^+ \approx 30$. These configurations resulted in total cell counts of approximately 3.8 million, 19.5 million, and 44.5 million cells, respectively. The three global mesh configurations are denoted as Case 1, Case 2, and Case 3, corresponding to coarse, medium, and fine grid resolutions, respectively.

To isolate the influence of near-wall resolution, an additional set of simulations was conducted with the bulk mesh resolution fixed at D/Δx = 100. In contrast, the wall-adjacent prism-layer resolution was varied to achieve target values of $y^+ \approx 1,5,10, and\ 30$ at cavitation inception. Local mesh refinement was applied in a dedicated refinement region extending approximately 2D×2D×12D around the sphere and in the downstream wake region.

This strategy ensured that the regions most relevant to cavity formation, shedding, and collapse were sufficiently resolved while maintaining computational efficiency. The primary objective of the grid refinement study was not simply to demonstrate monotonic improvement in accuracy with increasing resolution, but rather to quantify the sensitivity of collapse intensity and pressure response to spatial discretization. This analysis established a physically consistent resolution baseline for subsequent compressible and acoustic simulations.

At the inflow boundary, a uniform velocity was prescribed, while the outlet static pressure was adjusted to achieve the target cavitation number. Slip boundary conditions were applied to the lateral, top, and bottom tunnel walls to reduce confinement effects, and the sphere surface was modeled as a no-slip wall to resolve boundary-layer development and cavitation inception accurately.

While the incompressible simulations were performed using the baseline domain corresponding to the experimental test section, the computational domain in the compressible cases was extended both in the downstream and lateral directions. The downstream extension provides sufficient space for the propagation of collapse-induced pressure waves. At the same time, the lateral enlargement reduces artificial confinement and minimizes reflection of pressure disturbances from the side boundaries. In compressible simulations, outlet boundary conditions were defined allow pressure disturbances to leave the domain. A more detailed evaluation of non-reflecting boundary conditions is planned for future investigations.

The upstream length was kept identical to the experimental configuration to preserve the inflow development, and the near-sphere region where cavitation forms were maintained unchanged. The domain enlargement was therefore introduced primarily to improve acoustic-wave transmission rather than to modify the cavitation dynamics themselves.

Governing equations and Numerical Methodology

The cavitating flow was modeled by solving the unsteady multiphase Navier–Stokes equations within a finite-volume framework. Both incompressible and compressible formulations were considered to quantify the role of compressibility in cavitation dynamics and pressure-wave propagation.

The conservation equations for mass and momentum are written in a mixture form,

$$\frac{\partial \rho}{\partial t} + \nabla \cdot (\rho u) = \dot{m}, \quad (2)$$

$$\frac{\partial (\rho u)}{\partial t} + \nabla \cdot (\rho u \otimes u) = -\nabla p + \nabla \cdot \left[\mu_{eff}(\nabla u + \nabla u^T)\right] + \rho g, \quad (3)$$

where ρ is the mixture density, u is the velocity vector, p is the pressure, and $\mu_{eff} = \mu + \mu_t$ denotes the effective dynamic viscosity including laminar and turbulent contributions. The source term $\dot{m}$ represents the volumetric mass transfer source term from cavitation, and gravity g is included. For the compressible formulation, the total specific energy is also considered but left out here for brevity.

The mixture density and viscosity were evaluated using a volume-fraction formulation, where α_l and α_v denote the liquid and vapor volume fractions, respectively.

$$\rho = \alpha_l \rho_l + \alpha_v \rho_{v,} \quad (4)$$

$$\mu = \alpha_l \mu_l + \alpha_v \mu_v. \quad (5)$$

For compressible simulations, density was allowed to vary with pressure according to the equation of state using the physical speed of sound of water, enabling the propagation of acoustic disturbances. In contrast, for incompressible simulations, density was treated as constant and used as a baseline for comparison. Convective terms were discretized using second-order accurate schemes to reduce numerical diffusion and preserve unsteady cavitation structures such as shedding and collapse, while diffusive terms were discretized using central differencing. Time integration was performed using a second-order implicit scheme, and the time step was selected to maintain the Courant number below approximately 0.5 to ensure numerical stability.

Turbulence effects were modeled using the Improved Delayed Detached Eddy Simulation (IDDES) approach in combination with the Spalart–Allmaras (S–A) model. The hybrid IDDES formulation enables RANS behavior in the near-wall region and LES-like resolution in separated flow regions and shear layers, which are critical for capturing unsteady cloud cavitation dynamics and wake instabilities (Spalart et al., 1994; Spalart et al., 2006; Shur et al., 2008).

To ensure consistency in the comparative analysis, the same turbulence modeling strategy (IDDES with S–A closure) was employed in both OpenFOAM and STAR-CCM+ for the incompressible simulations. Maintaining identical turbulence treatment across solvers minimizes model-induced discrepancies and allows the observed differences to be attributed primarily to solver formulation, compressibility effects, and numerical implementation.

The transport equation for the modified turbulent viscosity $\tilde{\nu}$ is given by Eq. (6), where ν is the molecular kinematic viscosity, d is the wall distance, $\tilde{S}$ is a modified vorticity/strain-rate magnitude, and $C_{b1}, C_{b2}, C_{\omega 1}, \sigma$ are model constants; f_{t2} and f_ω are standard S-A damping functions. In IDDES, the wall distance d is replaced by a hybrid length scale d_{IDDES} that transitions from RANS behavior near the wall to LES-like behavior in separated regions, shown in Eq. (7), where Δ is a local grid length scale.

$$\frac{\partial \tilde{\nu}}{\partial t} + u \cdot \nabla \tilde{\nu} = C_{b1}(1 - f_{t2})\tilde{S}\tilde{\nu} + \frac{1}{\sigma}[\nabla \cdot \left((\nu + \tilde{\nu})\nabla \tilde{\nu} + C_{b2}(\nabla \tilde{\nu})^2\right] - C_{\omega 1} f_\omega \left(\frac{\tilde{\nu}}{d}\right)^2 \quad (6)$$

$$\tilde{d} = \max\left(\tilde{f_d}(1 + f_e)L_{RANS} + \left(1 - \tilde{f_d}\right)L_{LES}, SMALL\right) \quad (7)$$

In the incompressible solvers, the liquid–vapor interface was represented using a transport equation-based volume-fraction formulation coupled with the Schnerr–Sauer cavitation model (Sauer et al., 2000; Schnerr et al., 2001),

$$\frac{\partial \alpha_v}{\partial \mathrm{t}} + \nabla \cdot (\alpha_v u) = \frac{\dot{m}_{vap} - \dot{m}_{cond}}{\rho_v} \quad (8)$$

where $\dot{m}_{vap}$ and $\dot{m}_{cond}$ represent vaporization and condensation source terms, and ρ_v is the vapor density. In the Schnerr–Sauer model, interphase mass transfer is linked to a simplified bubble dynamics formulation. Vaporization and condensation rates depend on local pressure deviations from the saturation vapor pressure and on an assumed representative bubble radius,

$$\dot{m}_{lv} = \frac{\rho_v \rho_l}{\rho_m} \alpha_g (1 - \alpha_g) \frac{3}{R_B} \sqrt{\frac{2}{3} \frac{(p_v - p)}{\rho_l}}, p_v > p \quad (9)$$

$$\dot{m}_{vl} = \frac{\rho_v \rho_l}{\rho_m} \alpha_g (1 - \alpha_g) \frac{3}{R_B} \sqrt{\frac{2}{3} \frac{(p - p_v)}{\rho_l}}, p_v < p \quad (10)$$

where p_v is the saturation vapor pressure, R_b is the representative bubble radius, and ρ_l and ρ_v are the liquid and vapor densities, respectively. The bubbles are assumed to be spherical, and their radius is estimated from the local vapor volume fraction and a prescribed bubble number density $n = 1.0 \times 10^{11}\ \mathrm{m}^{-3}$.

The model assumes that bubbles neither form nor dissolve during the process. Water and water vapor were used as working fluids, with properties listed in Table 1. In the STAR-CCM+ simulations, an interface-compression scheme was employed as the default option, whereas the OpenFOAM simulations were performed as a mixture, i.e., without additional interface-compression treatment. As the simulations concern cloud cavitation without resolving bubble interfaces, the latter approach is appropriate, and no negative effects of interface sharpening in STAR-CCM+ were observed.

Baseline incompressible flow simulations were performed using IDDES with the S–A closure and the Schnerr–Sauer cavitation model in both OpenFOAM and STAR-CCM+. Maintaining consistent physical models and boundary conditions across both platforms enables assessment of solver- and numeric-related effects. The incompressible formulations are used to (i) establish the cavitation topology and shedding behavior, (ii) perform grid dependency studies efficiently, and (iii) conduct tool comparison under controlled conditions.

Compressible simulations were conducted using the *dbnsCavitatingFoam* solver in OpenFOAM (Arabnejad and Bensow, 2020) to investigate the effects of compressibility on transient pressure pulses and their propagation. This is a density-based solver that adopts the thermodynamic equilibrium mixture approach to model the presence of and phase transitions between liquid and vapor phases. This formulation allows density variations and finite wave-speed effects to be resolved, which is essential for acoustic-oriented analysis.

For acoustic source analysis, several permeable integration surfaces were defined around the cavitating region for use in the FW-H formulation. To assess the sensitivity of acoustic predictions to the definition of the source region, multiple surface configurations were considered. These include an enclosing ellipsoidal surface around the sphere, a short cylindrical surface, a longer cylindrical surface extending further downstream, and a wider cylindrical surface covering a larger portion of the wake region. In addition, pressure signals were recorded at selected monitoring locations in both near-field and far-field regions. A sampling duration was chosen to ensure statistically converged spectral results, and the recorded pressure time histories were subsequently processed using power spectral density (PSD) analysis. Figure 2 illustrates the permeable integration surfaces used in the FWH analysis, together with the location of the far-field receiver. These configurations are used in the subsequent sections to examine how the spatial extent and placement of the integration region influence the predicted acoustic source strength.

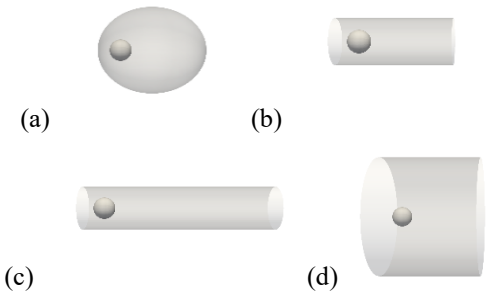

Figure 2: Permeable integration surfaces used for FWH acoustic analysis.
(a) enclosing an ellipsoidal surface surrounding the cavitating region,
(b) short cylindrical surface around the sphere,
(c) long cylindrical surface extending downstream,
(d) wide cylindrical surface covering a larger portion of the wake.

RESULTS AND ANALYSIS

Validation and Grid resolution effects on cavitation dynamics

The numerical framework is first validated against available experimental measurements using key global cavitation indicators, namely the cavity length and inception angle. Table 2 summarizes the predicted cavity length (L/D) and inception angle obtained using different grid resolutions and solvers. For all configurations, the predicted cavity length remains close to the experimental reference value of approximately L/D ≈ 2.7, indicating that the global cavity extent is captured with good accuracy. In contrast, the inception angle shows a stronger dependence on near-wall resolution. While variations in global cell size led to only moderate changes in L/D, systematically refining the wall-adjacent cells shifts the predicted inception angle. Overall, agreement in cavity length and consistent trends in inception angle provide confidence that the simulations reproduce the dominant cavitation topology and onset behavior with sufficient accuracy for subsequent pressure and acoustic analyses. Both solvers predict comparable cavity lengths with similar trends across grid resolutions, indicating robust large-scale predictions despite differences in numerical implementation.

Table 2: Predicted cavity length and inception angle for different solvers and grid configurations.

	STAR-CCM+		OpenFOAM	
	L/D	$\theta_{inception}$	L/D	$\theta_{inception}$
Case 1	2,72	68,9	2,60	75,1
Case 2	2,73	74,9	2,61	76,6
Case 3	2,95	76,3	2,71	76,6
y+ ~ 10			2,69	74,7
y+ ~ 5			2,71	73,6
y+ ~ 1			2,70	72,2

As an initial step, the computational cost associated with the baseline incompressible IDDES simulations was assessed. For comparable grid resolutions under the present configurations, STAR-CCM+ required a higher computational cost than OpenFOAM. At the finest resolution level, STAR-CCM+ required approximately 45 CPU hours using 256 cores, whereas OpenFOAM completed the corresponding simulation in approximately 15 CPU hours using 32 cores. Although computational efficiency was not the primary objective of the present study, this comparison is relevant for subsequent grid refinement and acoustic simulations.

The cavitation regime at $\sigma = 0.4$ was selected for detailed analysis, as it lies close to the transition toward supercavitation and exhibits elongated cavities with intermittent collapse activity, making it a demanding yet acoustically relevant test case.

Figure 3 compares experimental high-speed visualizations (left), reproduced from the reference study, with numerical predictions of iso-surfaces of vapor volume fraction at 0.9 (right) at $\sigma = 0.4$. The figure presents a time-resolved sequence illustrating the characteristic evolution of cloud cavitation around the sphere: cavity growth, instability induced by the re-entrant jet, cloud shedding, and subsequent breakup and collapse. Both experiment and simulation show a similar progression of the cavitation cycle. The sequence begins with the growth of an attached cavity on the sphere surface. As the cavity extends downstream, instabilities develop near the closure region, often associated with a re-entrant jet. This process leads to the detachment of large vapor structures, followed by cloud shedding into the wake. The detached vapor clouds subsequently undergo break-up into smaller fragments and collapse downstream, generating localized pressure pulses.

The numerical results reproduce the large-scale cavity shape, spatial extent, and temporal ordering of the growth–shedding–collapse process with good qualitative agreement. Differences are mainly observed in the fine-scale fragmentation and collapse structures, which are sensitive to spatial resolution and modeling details. These grid-dependent effects are examined further in the following sections through analysis of pressure fluctuations and acoustic response. This comparison confirms that the numerical framework captures the dominant mechanisms governing cloud cavitation dynamics prior to detailed pressure and acoustic analyses.

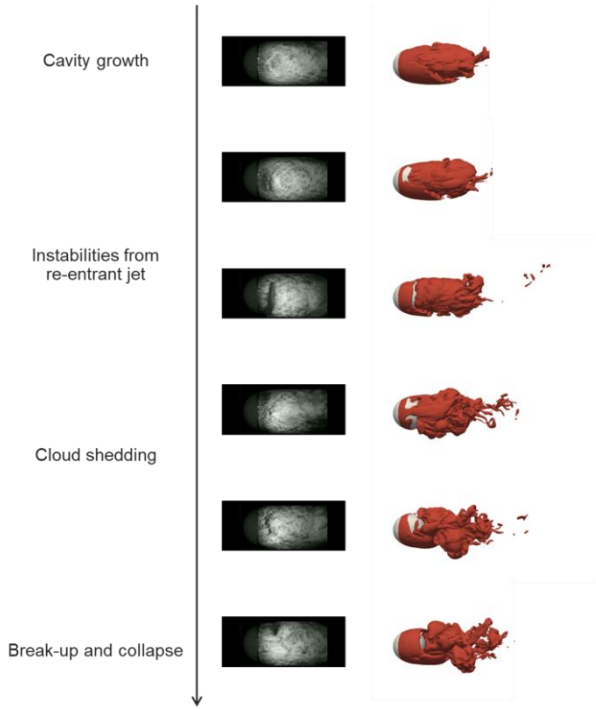

Figure 3: Comparison between experimental high-speed visualizations (left, reproduced from Brander et al.) and numerical predictions (right) of vapor volume fraction iso-surfaces during one cavitation cycle at $\sigma = 0.4$.

Figure 4 presents instantaneous mid-plane velocity magnitude contours for three global grid resolutions: (a) Case 1, (b) Case 2, and (c) Case 3. Across all cases, the large-scale wake structure and cavity extent are consistently reproduced, indicating that the global flow topology is relatively insensitive to grid resolution once a minimum level of refinement is achieved. However, clear differences emerge in the representation of smaller-scale flow features. As the grid is refined, increasingly fine-scale instabilities become visible along the cavity interface and within the separated shear layer downstream of the sphere.

On the coarse grid, these structures appear relatively smooth and diffuse, whereas the finer grids capture more fragmented and irregular flow patterns associated with shear-layer breakdown and wake unsteadiness. These small-scale structures are expected to play a critical role in the localization and intensity of collapse-induced pressure fluctuations. Improved resolution of interface disturbances and shear-layer instabilities enhance the representation of vapor fragmentation and collapse processes, which directly influence pressure pulse generation and the broadband acoustic emissions discussed in the following sections.

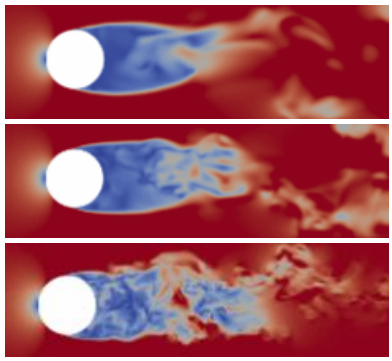

Figure 4: Instantaneous mid-plane velocity magnitude contours for different global grid resolutions: (a) Case 1, (b) Case 2, and (c) Case 3.

Collapse-Induced pressure field

To further investigate the influence of grid resolution on collapse dynamics, the instantaneous pressure field was examined together with the vapor cavity topology. Figure 5 shows vapor volume fraction iso-surfaces superimposed on mid-plane pressure contours for the three grid resolutions: (a) coarse, (b) medium, and (c) fine. The highlighted region indicates the primary collapse-active zone downstream of cavity closure. Strong pressure fluctuations are observed near the cavity closure, where interaction between the re-entrant jet and the cavity interface produces localized pressure peaks. Further downstream, detached vapor clouds are convected into the wake region, where breakup and subsequent collapse generate additional pressure disturbances. Clear resolution-dependent differences emerge. On the coarse grid, collapse regions appear relatively diffuse, and pressure peaks are spatially smeared. This behavior indicates that collapse events are under-resolved, leading to a broader distribution of pressure fluctuations. As the grid resolution increases, collapse structures become more localized and sharper pressure gradients are captured. On the finest grid, pressure peaks are more concentrated and exhibit higher local amplitudes, reflecting the improved resolution of small-scale vapor fragmentation and collapse events.

These results demonstrate that grid refinement does not significantly alter the global cavity extent but strongly affects the localization and intensity of collapse-driven pressure pulses. This has direct implications for acoustic prediction, as an accurate representation of collapse intensity is essential for resolving broadband pressure fluctuations. The spatial concentration of pressure peaks observed on finer grids provides a direct physical basis for the differences in RMS (dp/dt) distributions and spectral content discussed in the following sections.

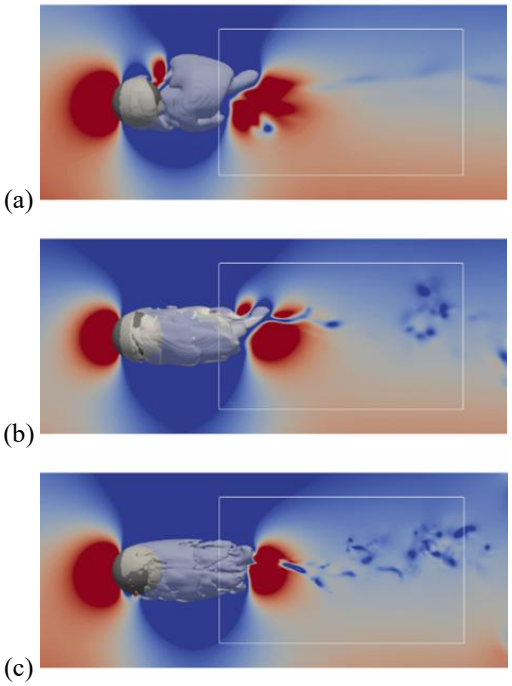

Figure 5: Vapor cavity iso-surfaces superimposed on mid-plane pressure contours for different global grid resolutions: (a) Case 1, (b) Case 2, and (c) Case 3.

For quantitative assessment, a collapse-active region encompassing the cavity closure and near-wake zone was defined, and pressure probes were placed within this region. From the recorded pressure signals, the root-mean-square of the pressure time derivative, RMS (dp/dt), was computed. The temporal derivative is used because cavitation collapse is highly impulsive, characterized by rapid pressure rises over short time scales; RMS (dp/dt) therefore provides a sensitive measure of collapse intensity and is closely linked to broadband noise generation mechanisms.

Figure 6 shows mid-plane contours of RMS (dp/dt) for the three grid resolutions. At first glance, the coarse grid produces broader regions of elevated RMS levels and a more spatially distributed pattern. However, this should not be interpreted as indicating physically stronger or more widespread collapse. Rather, on the coarse grid, individual collapse events are under-resolved both temporally and spatially, leading to smeared pressure peaks that are distributed over a larger region. This produces a more diffuse and, in a global sense, seemingly "louder" field. With increasing grid resolution, the collapse dynamics become more sharply resolved. On the finer grids, high RMS (dp/dt) values appear more localized, concentrated near the cavity closure and in the near-wake, where detached vapor clouds collapse. This increased localization reflects the ability of the refined mesh to capture short-lived, spatially confined pressure peaks associated with

individual collapse events rather than spreading them artificially over a larger area. The observed spatial asymmetry in the RMS (dp/dt) field is consistent with the inherently unsteady, three-dimensional nature of cloud cavitation, in which shedding and collapse do not occur at perfectly symmetric locations from cycle to cycle. Some contribution from finite sampling duration cannot be entirely excluded; however, the overall structure and location of the high-intensity regions remain consistent across grid resolutions, suggesting that the dominant patterns are physically meaningful.

Overall, the results indicate that grid refinement influences not only cavity morphology but also how collapse-driven pressure pulses are represented in space: coarser grids tend to smear and spatially distribute collapse intensity, whereas finer grids resolve more localized and physically concentrated collapse regions. This has direct implications for the prediction and interpretation of cavitation-induced pressure fluctuations and associated noise generation.

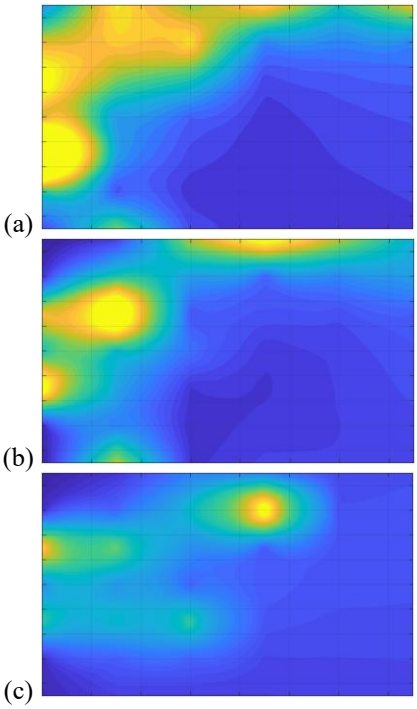

Figure 6: Mid-plane contours of RMS(dp/dt) for different global grid resolutions: (a) Case 1, (b) Case 2, and (c) Case 3.

To further examine the influence of grid resolution on collapse dynamics, pressure signals recorded inside the collapse-active region were analyzed in the frequency and time domains. Figure 7 presents the one-third octave spectra of the pressure fluctuations obtained using the coarse, medium, and fine grids.

The spectra exhibit broadband energy across a wide frequency range, consistent with the impulsive nature of cavitation collapse. As the grid resolution increases, spectral levels rise, particularly in the mid- and high-frequency ranges, indicating that finer grids resolve sharper collapse events and stronger pressure gradients.

In contrast, the coarse grid shows reduced high-frequency content, suggesting under-resolution of rapid collapse processes. The temporal characteristics show a consistent trend. With grid refinement, the pressure signals exhibit clearer quasi-periodic behavior associated with the cloud-shedding cycle, reflecting improved temporal fidelity in the simulated collapse dynamics. These effects are most pronounced near the cavity closure region ($x \approx 1.2D$), where collapse activity is strongly influenced by the re-entrant jet interaction.

Further downstream, collapse becomes more intermittent and less organized, leading to reduced temporal coherence and broader spectral content. Overall, these results indicate that grid refinement plays a critical role in resolving both the intensity and temporal structure of collapse-induced pressure fluctuations, which is essential for reliable acoustic analysis.

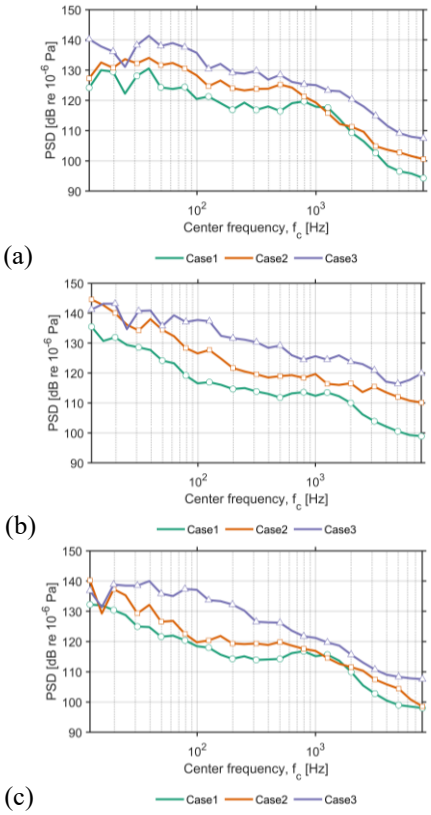

Figure 7: One-third octave spectra of pressure fluctuations recorded inside the collapse-active region for different grid resolutions: (a) near the cavity closure region, (b) intermediate downstream location, and (c) further downstream in the wake. Results are shown for Cases 1, 2, and 3.

Taken together, these results demonstrate that grid refinement influences both the spectral distribution and temporal structure of collapse-induced pressure fluctuations. Finer grids not only increase the resolved energy at higher frequencies but also improve the representation of both quasi-periodic and intermittent features of cloud cavitation.

This provides a more physically consistent basis for subsequent acoustic analyses, as accurate resolution of localized collapse dynamics is essential for reliable prediction of broadband noise generation and identification of dominant source regions.

Acoustic source analysis in Incompressible flow

To investigate how collapse dynamics are reflected in acoustic source representations within the incompressible framework, a comparative analysis was conducted between three quantities: a volume-based source proxy, raw pressure recorded on permeable integration surfaces, and far-field acoustic pressure predicted using the FWH method. The far-field receiver is located 10 m downstream of the sphere center. To interpret collapse-driven pressure generation in a physically intuitive manner, a global source proxy based on bubble dynamics theory was introduced. In classical bubble dynamics theory, the radiated acoustic pressure is proportional to the second time derivative of the bubble volume. For a spherical source, this relationship can be expressed as

$$p_A(t) = \frac{\rho_L}{4\pi\ell}\frac{d^2V(t)}{dt^2} \qquad (13)$$

where ρ_L is the liquid density, $V(t)$ is the instantaneous vapor volume, and ℓ is the distance from the source to the observation point (Fitzpatrick et al., 1956; Ceccio et al., 1991). This relation indicates that rapid volume changes during collapse act as primary acoustic sources.

Based on this concept, the global vapor volume within the cavitating region was spatially integrated and differentiated twice in time to obtain a volume-acceleration signal. The resulting quantity was scaled by the factor $\rho_L/(4\pi l)$ so that its magnitude is consistent with pressure units, enabling direct comparison with surface pressure signals and FWH-derived acoustic predictions.

Since numerical differentiation amplifies high-frequency numerical noise, the cavity volume signal was smoothed prior to computing the volume acceleration. A locally weighted regression (LOWESS) filter was applied to the raw vapor-volume time series to preserve the main temporal characteristics while suppressing high-frequency numerical fluctuations. This approach follows previous studies that applied smoothing to ensure stable evaluation of volume-acceleration-based acoustic source proxies (Muye et al., 2022; Qais Shehadah et al., 2026).

Power spectral densities (PSDs) of three quantities were compared: the volume-based source proxy (scaled d squared, cap V over d t squared), the raw pressure integrated over the permeable FWH surface, and the radiated pressure predicted at a receiver located 10 m downstream using the FWH formulation.

Figure 8 compares the ì three quantities: considering the FWH formulation for different surface geometries: (a) an enclosing ellipsoidal surface, (b) a short cylindrical surface around the sphere, (c) a longer cylinder extending further downstream, and (d) a large cylinder covering a wider portion of the wake region.

Across all configurations, the spectra exhibit broadband characteristics typical of collapse-driven cavitating flows, with energy distributed over a wide frequency range. The spectral trends remain similar across different surface geometries, indicating that the dominant unsteady dynamics associated with cloud shedding and collapse are consistently captured.

Comparing the three quantities highlights the different physical roles they represent. The volume-acceleration signal is directly linked to the global vapor-volume dynamics and therefore reflects the strength and temporal evolution of collapse activity. In contrast, the FWH-predicted pressure corresponds to the radiated response at the observation point after propagation effects are accounted for. The similarity in spectral content in the low- and mid-frequency ranges can be attributed to the global shedding cycle, which governs the large-scale variation of vapor volume and consequently dominates the source dynamics.

In contrast, the pressure integrated over the permeable surface consistently exhibits higher spectral levels and stronger high-frequency content. This behavior is expected, as the surface-integrated signal captures near-field impulsive collapse activity. In contrast, the FWH prediction represents the radiated acoustic response at a downstream far-field receiver, where high-frequency components are partially attenuated and spatially filtered during propagation.

Differences between the integration of surface geometries appear mainly in the predicted amplitude rather than in the spectral shape. The short cylindrical surface primarily encloses the collapse activity near the cavity-closure region, whereas the long and large cylindrical surfaces extend further into the wake where detached vapor clouds continue to evolve and collapse. As a result, the downstream-extending surfaces may show slightly elevated spectral levels, which can be associated with the inclusion of additional wake-related pressure fluctuations. However, this increase does not necessarily imply improved source representation but rather reflects the influence of the spatial extent of the integration surface on the captured pressure field.

This dependence on surface extent suggests that collapse-related pressure sources are not confined to a single localized region near the cavity closure but may be distributed along the streamwise direction of the wake. Despite these geometric differences, the persistence of similar spectral trends across all configurations indicates that global cavitation dynamics govern the dominant acoustic source mechanisms.

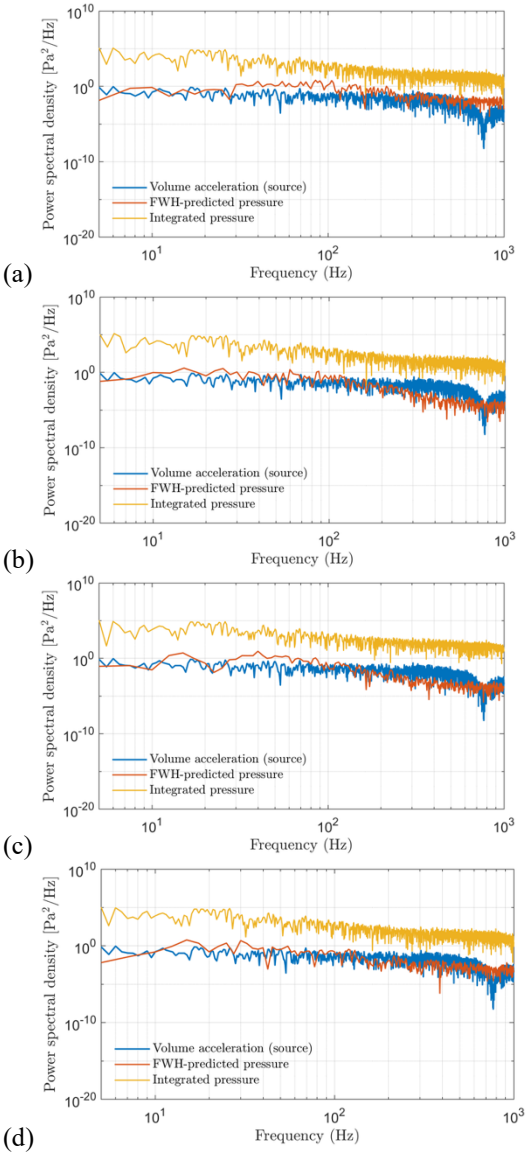

Figure 8: Comparison of power spectral densities of the volume-acceleration-based source proxy, integrated pressure on permeable-surface pressure, and FWH-predicted far-field pressure for different permeable integration surface configurations: (a) enclosing ellipsoidal surface, (b) short cylinder, (c) long cylinder, and (d) wide cylinder.

Figures 9 and 10 illustrate the influence of receiver location on the predicted acoustic spectra for two permeable integration surface configurations: a long cylindrical surface and an enclosing ellipsoidal surface. Three receiver positions are considered: (a) a downstream far-field location, (b) a lateral location at the sphere center plane, and (c) an oblique position located both downstream and laterally offset.

For both surface configurations, the volume-acceleration-based signal and the surface-integrated pressure remain independent of receiver position, as they represent global source-side quantities. In contrast, the FWH-predicted pressure varies with observer location due to propagation and observation-geometry effects.

At the downstream far-field location, the predicted spectrum reflects the cumulative contribution of collapse events convected along the wake centerline. At the lateral receiver position, the overall spectral levels are reduced, and minor changes in spectral distribution are observed, which are primarily attributed to geometric spreading and the observation angle rather than to strong intrinsic directivity. The oblique receiver position exhibits intermediate characteristics.

Across all receiver locations, the spectra retain broadband features typical of collapse-driven cavitation dynamics. The spectral shape of the volume-acceleration signal remains consistent with the FWH-predicted pressure in the low- and mid-frequency ranges, indicating that global vapor-volume variations dominate the source dynamics. However, the amplitude and detailed spectral distribution of the FWH signal depend on observer position, reflecting propagation effects and the spatial extent of the source region.

Although both the long cylindrical and ellipsoidal integration surfaces fully enclose the primary cavitation region, differences emerge in how receiver-location sensitivity is manifested in the predicted spectra. Since both surfaces capture the main cavitation activity, these differences are not interpreted as resulting from the inclusion of additional source regions, but rather from how the spatial distribution of pressure fluctuations is represented and integrated over each surface.

The ellipsoidal surface tends to emphasize the immediate collapse region near the sphere. In contrast, the long cylindrical surface extends further into the wake and includes a more distributed region of convected collapse activity. This may lead to slight differences in how the spatially distributed source field is projected into the far-field response. Overall, the results suggest that receiver-location sensitivity is influenced more by propagation geometry and surface definition than by changes in the underlying source mechanism itself.

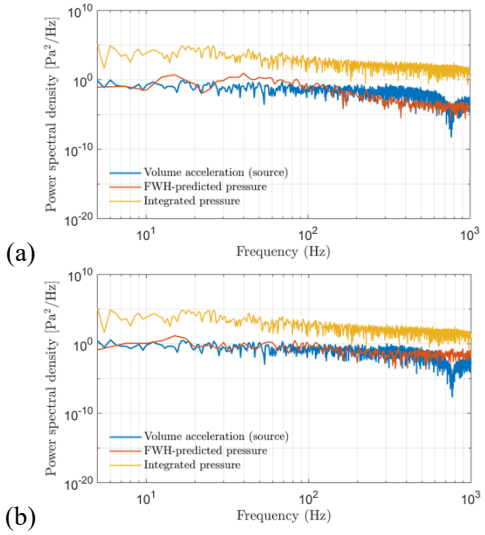

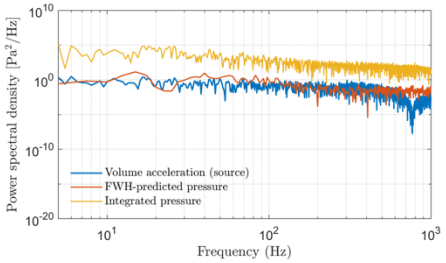

(c)

Figure 9: PSDs of the volume-acceleration-based source proxy, surface-integrated pressure, and FWH-predicted acoustic pressure for different receiver locations using the long cylindrical permeable integration surface.

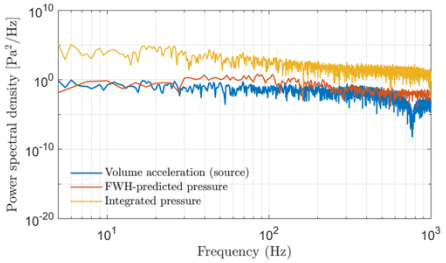

(a)

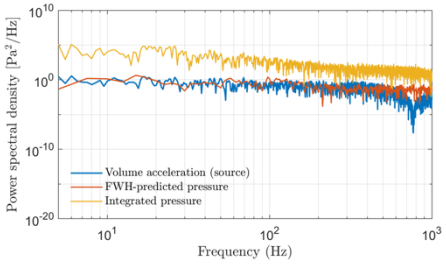

(b)

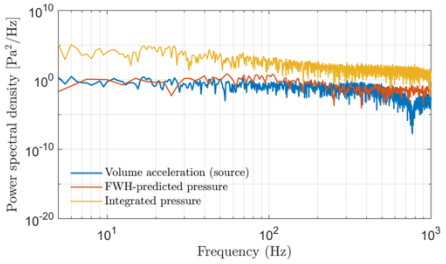

(c)

Figure 10: PSDs of the volume-acceleration-based source proxy, surface-integrated pressure, and FWH-predicted acoustic pressure for different receiver locations using the enclosing ellipsoidal permeable integration surface.

The incompressible analysis provides insight into the relationship between cavitation dynamics, collapse-induced pressure fluctuations, and their representation through acoustic source proxies. However, since incompressible formulations do not resolve finite-speed pressure-wave propagation, the radiated acoustic field is only indirectly represented. To further investigate the role of compressibility in pressure-wave generation and transmission, the following section presents results obtained from fully compressible simulations.

Effects of Compressibility on pressure and acoustic response

To further examine the role of compressibility in acoustic prediction, Figure 11 presents a direct comparison between the far-field acoustic spectra obtained from incompressible and compressible simulations for the different permeable integration surfaces. The volume-acceleration-based spectrum is shown as a reference to represent the global collapse dynamics extracted from the flow field.

Although all surfaces fully contain the collapse-active region, noticeable differences in the predicted spectral levels indicate that the FWH results are sensitive to the geometry and extent of the permeable integration surface. This sensitivity is most pronounced on the long cylindrical surface, which consistently yields higher spectral levels across a broad frequency range than the other configurations. This behavior can be attributed to the extended downstream coverage of the long cylinder. The higher levels observed for the long cylindrical surface suggest that the FWH prediction is sensitive to the axial extent of the permeable integration surface. While all surfaces enclose the primary collapse region, extending the surface further downstream modifies the balance between collapse-driven pressure waves and convected flow-induced fluctuations crossing the surface, leading to an increase in the predicted broadband content. The short cylinder and the ellipsoidal surface confine the integration region more tightly around the primary collapse zone, reducing the influence of downstream wake structures and resulting in more consistent spectral levels. The large-radius cylindrical surface exhibits comparatively stable behavior, suggesting that increasing the radial distance from the source region helps reduce contamination from near-field hydrodynamic pressure fluctuations. Clear differences are also observed between the incompressible and compressible formulations. The compressible FWH consistently predicts higher broadband levels, particularly in the mid- to high-frequency range, reflecting the role of compressibility in the transmission of collapse-induced pressure waves.

The incompressible formulation produces lower spectral levels and a more rapid decay at higher frequencies, consistent with its limited ability to represent true acoustic wave propagation. Despite these differences in magnitude, both formulations exhibit similar spectral trends across the various surface configurations, indicating that the dominant source dynamics remain consistent.

It shows that the predicted amplitude is influenced by the spatial extent of the integration surface, particularly downstream, where wake-related fluctuations are present, despite all permeable surfaces capturing the main characteristics of the collapse-driven acoustic response.

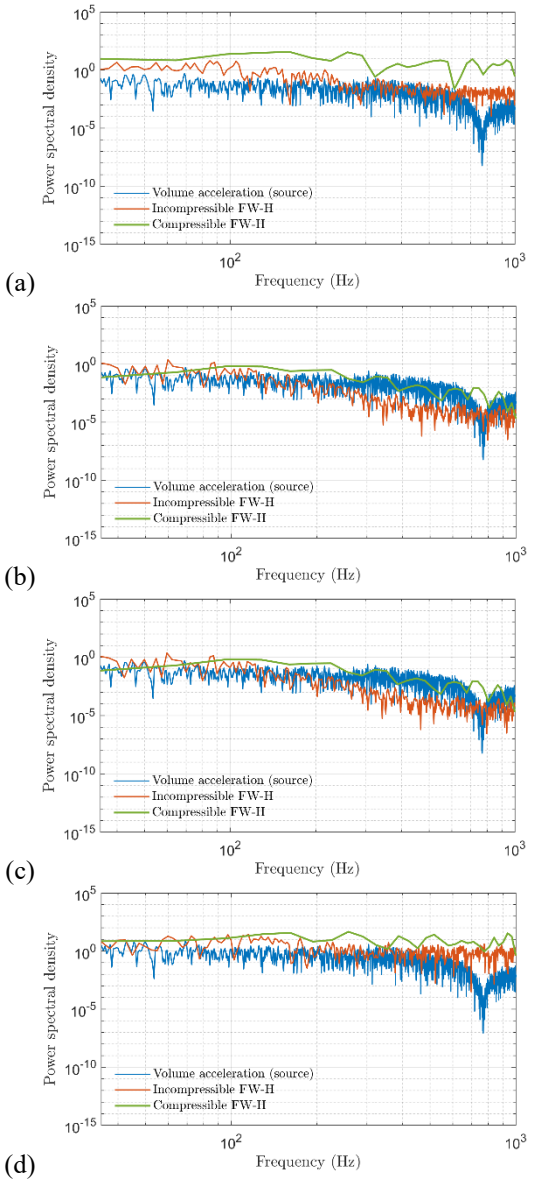

Figure 11: Comparison of FW-H predicted far-field spectra between incompressible and compressible formulations and volume-acceleration reference for different permeable integration surfaces: (a) enclosing ellipsoidal surface, (b) short cylinder, (c) long cylinder, and (d) wide cylinder.

CONCLUSIONS

This study presented a high-fidelity computational investigation of cloud cavitation around a sphere, with particular emphasis on the link between cavitation dynamics, collapse-induced pressure fluctuations, and the resulting acoustic signatures. The numerical framework was validated against experimental benchmark data, demonstrating good agreement in cavity length, inception behavior, and overall unsteady flow characteristics, confirming its ability to capture the primary features of cloud cavitation.

A systematic comparison between incompressible and compressible formulations showed that incompressible simulations reliably reproduce the overall cavitation topology and shedding dynamics, whereas the compressible formulation provides additional physical insight into transient pressure-wave propagation and localized collapse events. Resolving density variations and finite wave-speed effects was found to be essential for capturing sharp pressure pulses and the associated high-frequency pressure fluctuations generated during vapor-cloud implosion.

The analysis of pressure signals and spectral characteristics revealed a clear connection between localized collapse dynamics and the radiated acoustic response. Increased spatial resolution improved the representation of rapid volume changes and intensified pressure peaks, leading to stronger high-frequency spectral content. The results indicate that the dominant acoustic contribution is primarily governed by collapse-driven loading mechanisms, highlighting the importance of collapse intensity and localization in shaping the pressure-wave field.

Overall, the present work contributes to a clearer physical understanding of how collapse-induced pressure generation is linked to the acoustic response in cloud cavitating flows. The sphere configuration proved to be a suitable and controlled benchmark for isolating these mechanisms, and the findings provide a basis for improved prediction of cavitation-induced pressure fluctuations and for future investigations targeting acoustic characterization in more complex geometries and engineering applications.

ACKNOWLEDGEMENTS

This work is performed with the BluEcho project as part of the EC Sustainable Blue Economy Program.

The computations handling was enabled by resources provided by the National Academic Infrastructure for Supercomputing in Sweden (NAISS), partially funded by the Swedish Research Council through grant agreement no. 2022-06725.

REFERENCES

Arabnejad, Mohammad Hossein, Ali Amini, Mohamed Farhat, and Rickard E. Bensow. "Numerical and experimental investigation of shedding mechanisms from leading-edge cavitation." International journal of multiphase flow 119 (2019): 123-143.

Arabnejad, Mohammad Hossein, and Rickard E. Bensow. "dbnsCavitatingFoam: A density-based solver with equilibrium cavitation models in the OpenFOAM framework." arXiv preprint arXiv:2009.04744 (2020).

Brandner, P. A., G. J. Walker, P. N. Niekamp, and B. Anderson. "An experimental investigation of cloud cavitation about a sphere." Journal of Fluid Mechanics, 656 (2010): 147-176.

Brentner, Kenneth S., and Feri Farassat. "Analytical comparison of the acoustic analogy and Kirchhoff formulation for moving surfaces." AIAA journal, 36, no. 8 (1998): 1379-1386.

Ceccio, Steven L., and Christopher E. Brennen. "Observations of the dynamics and acoustics of travelling bubble cavitation." Journal of Fluid Mechanics, 233 (1991): 633-660.

Cheng, Xinsheng, Xueming Shao, and Lingxin Zhang. "The characteristics of unsteady cavitation around a sphere." Physics of Fluids, 31, no. 4 (2019).

De Graaf, K. L., P. A. Brandner, and B. W. Pearce. "Spectral content of cloud cavitation about a sphere." Journal of Fluid Mechanics, 812 (2017): R1.

Spalart, Philippe, and Steven Allmaras. "A one-equation turbulence model for aerodynamic flows." In 30th aerospace sciences meeting and exhibit, p. 439. 1992.

Farassat, F. *Theory of noise generation from moving bodies with an application to helicopter rotors*. No. L-10379. 1975.

Farassat, Fereidoun. *Derivation of Formulations 1 and 1A of Farassat*. No. L-19318. 2007.

Fitzpatrick, H. M., and M. Strasberg. "Hydrodynamic sources of sound." In Proc. 1st Symp. on Naval Hydrodynamics, Washington, DC, NAS-NRC Publ, vol. 515, pp. 241-280. 1957.

Ge, Muye, Urban Svennberg, and Rickard E. Bensow. "Investigations on prediction of ship noise using the FWH acoustic analogy with incompressible flow input." Ocean Engineering, 257 (2022): 111531.

Liu, Yun-qing, Wei Zhao, Zhi Pan, Zhi-pu Guo, Rui Yuan, and Qin Wu. "Investigation on the dynamic behavior of cloud cavitation around a flexible hydrofoil." Journal of Hydrodynamics, 35, no. 4 (2023): 712-723.

Hu, Ke, Ming-tai Song, Chao Ma, Yun-qiao Liu, and Ben-long Wang. "Characteristics of radiated noise from the cavitation flows around a NACA16012 twisted hydrofoil." Journal of Hydrodynamics, 37, no. 3 (2025): 449-467.

JE, Ffowcs Williams, and D. Hawkings. "Sound generated by turbulence and surfaces in arbitrary Motion Philos." TR Soc. A 264 (1969): 21-342.

Khraisat, Qais Shehadeh, Martin Persson, and Rickard E. Bensow. "Cavitation underwater radiated noise methodology applied to a propeller operating in-behind condition." Ocean Engineering, 349 (2026): 124084.

Kolahan, Arman, Ehsan Roohi, and Mohammad-Reza Pendar. "Wavelet analysis and frequency spectrum of cloud cavitation around a sphere." Ocean Engineering, 182 (2019): 235-247.

Pendar, Mohammad-Reza, and Ehsan Roohi. "Cavitation characteristics around a sphere: An LES investigation." International Journal of Multiphase Flow, 98 (2018): 1-23.

Sahu, P., P. M. V. Subbarao, and R. Goyal. "Exploring cloud cavitation and cavitation vortex dynamics with partially averaged Navier–Stokes turbulence models." Physics of Fluids, 37, no. 1 (2025).

Sauer, Jürgen, and Günter H. Schnerr. "Unsteady cavitating flow-a new cavitation model based on a modified front capturing method and bubble dynamics." In Proceedings of 2000 ASME fluid engineering summer conference, vol. 251, pp. 1073-1079. ASME, 2000.

Shur, Mikhail L., Philippe R. Spalart, Mikhail Kh Strelets, and Andrey K. Travin. "A hybrid RANS-LES approach with delayed-DES and wall-modelled LES capabilities." *International journal of heat and fluid flow* 29, no. 6 (2008): 1638-1649.

Spalart, P., S. Deck, M. L. Shur, K. D. Squires, M. Kh Strelets, and A. Travin. "A New Version of Detached-

Schnerr, Günter H., and Jürgen Sauer. "Physical and numerical modeling of unsteady cavitation dynamics." In Proceedings of the Fourth International Conference on Multiphase. Flow, New Orleans, USA, pp. 1-12. 2001.

Vikström, Marko, Urban Svennberg, Muye Ge, and Rickard E. Bensow. "The effect of porous data surface shape and size on ship noise prediction using the FWH acoustic analogy with incompressible solver for a cavitating propellers." In Proceedings of the 7th International Symposium of Marine Propulsors. 2022.

Wang, Changchang, Guoyu Wang, and Biao Huang. "Characteristics and dynamics of compressible cavitating flows with special emphasis on compressibility effects." International Journal of Multiphase Flow, 130 (2020): 103357.

Wang, Y-C., and Christopher E. Brennen. "The noise generated by the collapse of a cloud of cavitation bubbles." (1995).

Wilson, Miles, John R. Blake, and Peter M. Haese. "Cloud cavitation dynamics." The ANZIAM Journal, 50, no. 2 (2008): 199-208.

Zhao, Xiaotao, Ziyang Wang, Xiaorui Bai, Huaiyu Cheng, and Bin Ji. "Unsteady cavitation dynamics and pressure statistical analysis of a hydrofoil using the compressible cavitation model." Physics of Fluids, 35, no. 10 (2023).